Supplementary Information (SI) for Journal of Materials Chemistry A.
This journal is © The Royal Society of Chemistry 2026

Supporting information File

Facet-Dependent Oxygen Evolution on IrO_2 from Machine-Learned Potential Driven Atomistic Models

Swastik Laha, and Kalishankar Bhattacharyya*

Department of Chemistry, Indian Institute of Technology Guwahati

Guwahati 781039, Assam, India

Email: ksb@iitg.ac.in

Content:

1. Model Systems:

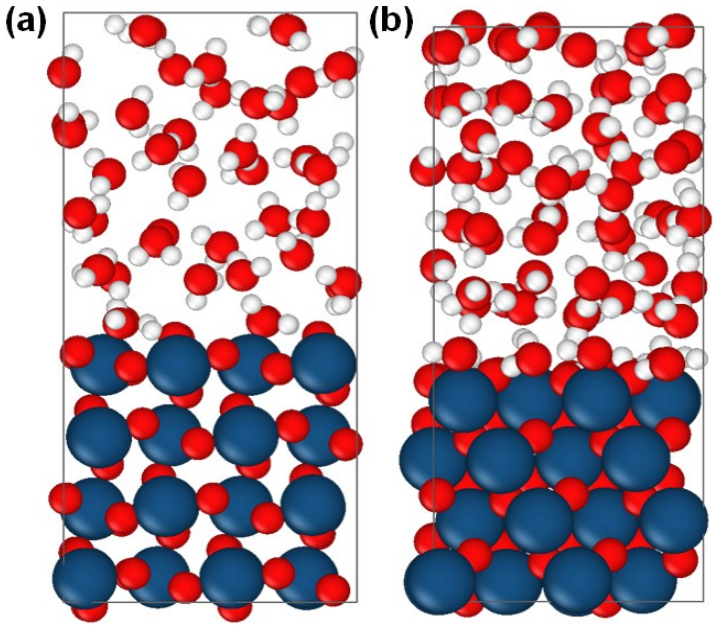

Figure S1: MLMD simulation equilibrated explicit water solvation slab models of the (a) (110) and (b) (101) facet of the IrO_2 surface.

2. Computational Details and Methodology:

A symmetric periodic slab composed of four O-Ir-O layers with lateral *xy* dimensions of 2 × 2 supercells was modelled to represent the rutile IrO_2 (110) and (101) surfaces. This resulted in a symmetric IrO_2 composition, i.e., for both surfaces, we had 32 Ir and 64 O atoms. The explicit aqueous IrO_2 (110) and (101) models were built up by keeping the slabs separated with a 15 Å solvent space. This led to the construction of an orthorhombic supercell with dimensions 6.35 × 12.74 × 26.99 Å3 and 11.03 × 9.01 × 24.39 $Å^3$, respectively. The vacuum layer was introduced between two periodic slabs along the surface normal, z-direction, in order to diminish/prevent the interactions between periodic, adjacent images. The solvent space between the slabs was filled with 41 and 63 water molecules for the (110) and (101) surfaces, respectively, including one monolayer of water (4 and 8 water molecules, respectively). These ensured the bulk region water density to be near 1 g/cm^3. All our simulations were carried out under charge-neutral conditions, corresponding to the point of zero protonic charge for the aqueous IrO_2.

2.1 AIMD Simulations:

We performed all the *ab-initio* molecular dynamics (AIMD) simulations using the Quickstep [1] code as implemented in the CP2K[2] package. Along all three directions, the periodic boundary conditions were applied to simulate an effectively infinite system. The Perdew-Burke-

Ernzerhof (PBE)[3] functional was coupled with the Grimme's D3[4] dispersion correction to simulate the IrO_2/H_2O interface accurately. To define the core electrons, we opted for the Goedecker-Teter-Hutter (GTH)[5,6] pseudopotential. The employed atomic basis sets for the valence electrons (H: $1s^1$; O: $2s^2$ and $2p^4$; Ir: $5s^2$, $5p^6$, $5d^7$, and $6s^2$) were the standard short-ranged double-basis functions with one set of polarization functions (DZVP) [7]. The plane wave cut-off for the electronic density expansions was set as 400 Ry. Furthermore, the target accuracy for the SCF convergence was set to 3×10^{-7} a.u. The canonical NVT ensemble was employed for the simulation with a time step of 0.5 fs. The simulations were carried out for 10 ps for each of the IrO_2/H_2O interface systems. The equilibrium temperature for all simulations was maintained at 330K to ensure a frank diffusive motion of liquid water, utilizing the Nosé-Hoover thermostat.[8]

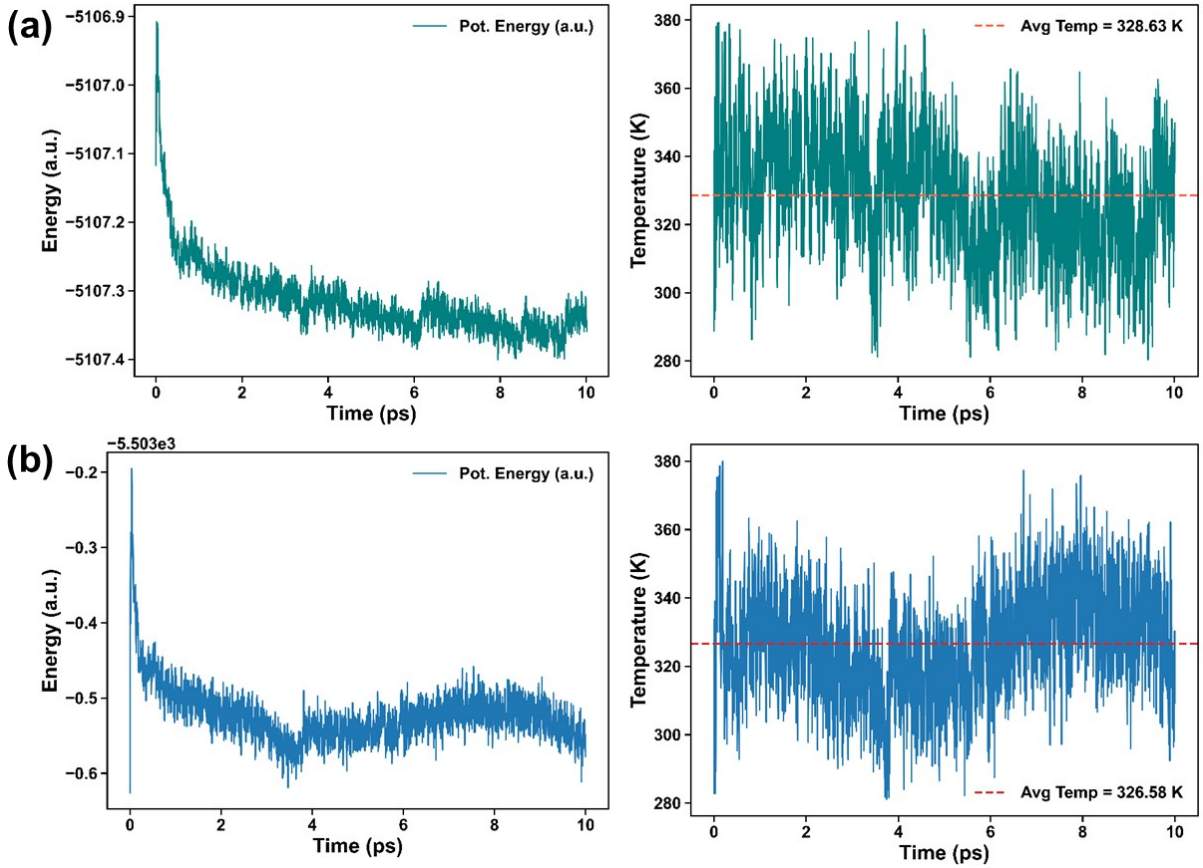

Figure S2: Time evolution of potential energy (left) and temperature (right). Panels (a) and (b) correspond to the (110) and (101) surfaces, respectively, obtained from the 10 ps AIMD simulations. The potential energy stabilizes over time, while the temperature fluctuates around the target value, confirming thermal stability of both surfaces during the simulation.

2.2 Machine learning Potential Training:

In this work, we trained the deep learning-based interatomic potentials using the open-source DeePMD-kit[9,10] package. The Deep Potential-Smooth Edition (DeepPot-SE)[11], a two-atom embedding descriptor model, was used to capture both angular and radial information of atomic configurations for the structural descriptor. The cut-off radius for neighbor searching within the local environment was set to 6.0 Å. The cut-off smooth was set as 0.5 Å. The embedding network had layers of size 25 × 50 × 100, and the fitting network used layers of size 240 × 240 × 240. The overall learning dataset for the (110)/H_2O and (101)/H_2O interfaces is constructed from their respective AIMD simulation trajectories. The 10 ps AIMD trajectory for each facet was systematically subsampled to yield 10,000 configurations per surface, rather than using all ~20,000 generated snapshots directly. A denser sampling interval was applied during the pre-equilibration regime (0-3 ps) to ensure adequate representation of higher-energy, structurally distorted configurations, while a comparatively sparser sampling frequency was employed over the equilibrated region (3-10 ps). An 80/20 train/validation split was subsequently applied to this subsampled dataset, yielding approximately 8,000 training configurations and 2,000 validation configurations per facet. This deliberate subsampling strategy was adopted to balance configurational diversity with computational efficiency, and to avoid redundancy arising from the high temporal correlation of consecutively generated AIMD frames. To certify the quality of MLMD simulations, we trained the inter-atomic deep potential with 1000000 batch steps. We achieved L2 energy error of 0.34 meV/atom and force error 81.60 meV/Å on the training set, as well as L2 error of 0.35 meV/atom and 82.22 meV/Å for the energy and force, respectively, on the validation set for the (110)/H_2O interface model. Similarly, for the (101)/H_2O interface model, we obtained an L2 energy error of 0.36 meV/atom and a force error of 90.19 meV/Å on the training set, followed by an energy error of 0.36 meV/atom and a force error of 90.39 meV/Å on the validation set.

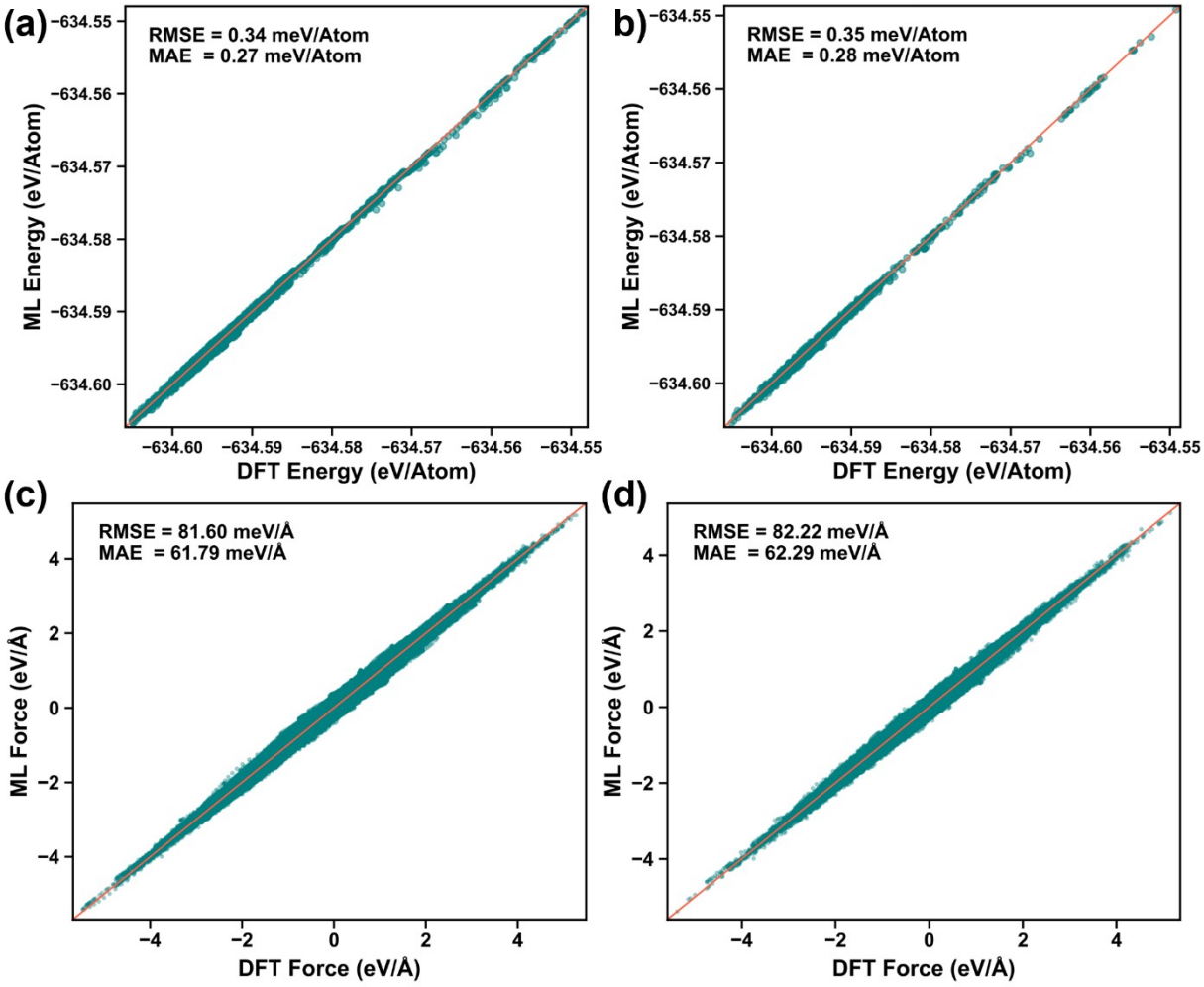

Figure S3: Parity plots of machine-learning (ML) predicted versus DFT reference energies (upper panel) and forces (lower panel). (a) and (c) show results for the training set; (b) and (d) show results for the validation set, for the IrO_2(110) surface. Energies are given in eV/atom and forces in eV/Å. The diagonal line indicates perfect agreement.

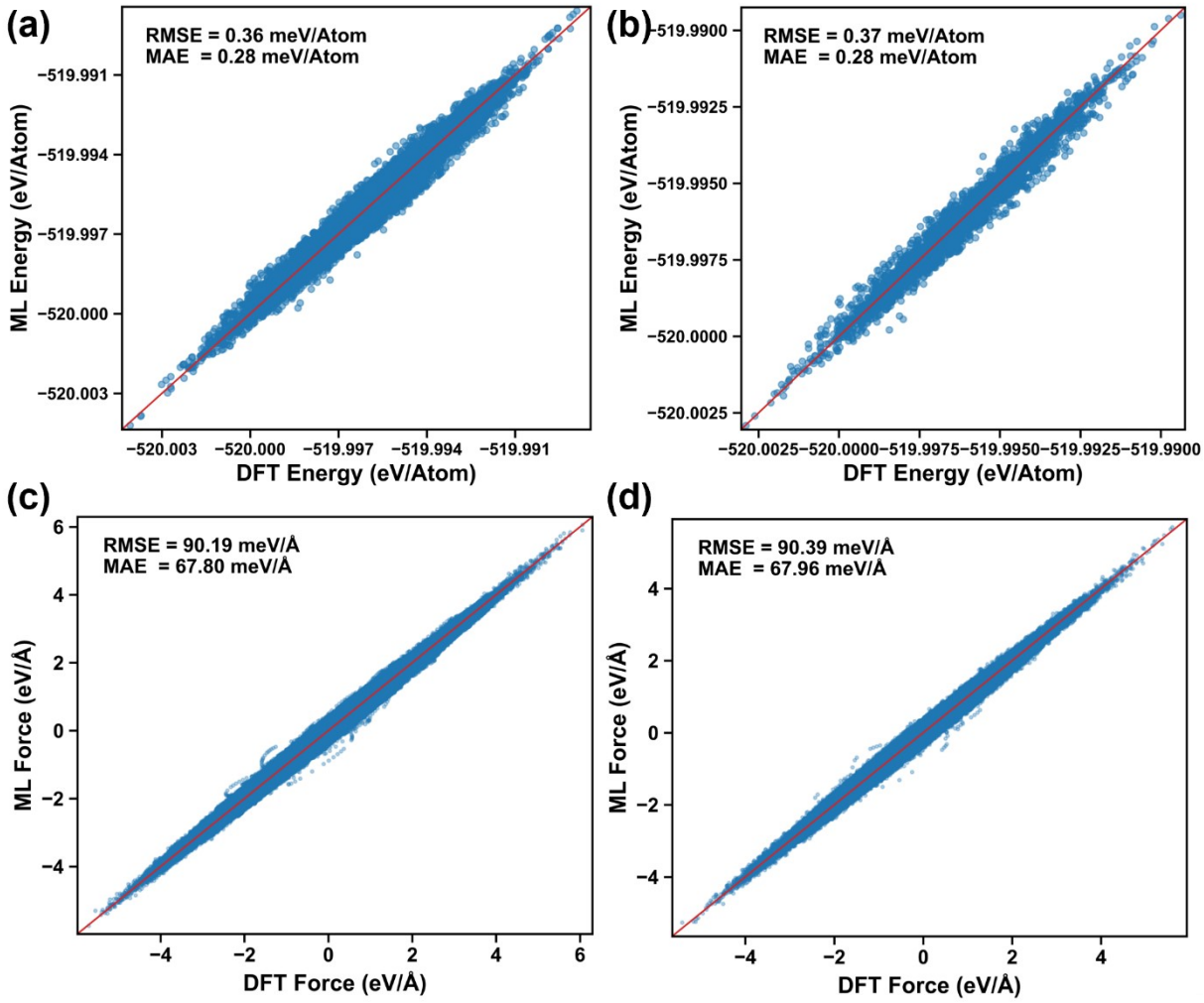

Figure S4: Parity plots of machine-learning (ML) predicted versus DFT reference energies (upper panel) and forces (lower panel). (a) and (c) show results for the training set; (b) and (d) show results for the validation set, for the IrO2(101) surface. Energies are given in eV/atom and forces in eV/Å. The diagonal line indicates perfect agreement.

2.3 MLMD Simulations:

We performed all potential-based MLMD simulations using the LAMMPS[12] code, interfaced with the DeePMD-kit. We kept the identical supercell model structure as implemented in the AIMD simulations for both the IrO_2/H_2O interface models. The simulations were carried out under constant volume, constant temperature, and canonical ensemble conditions. The temperature was also controlled here with the Nosé-Hoover thermostat at 330 K. The MD time step was set to 0.5 fs, and the total time scale of the MLMD simulations was 10 ns for each of the surface-water interface models.

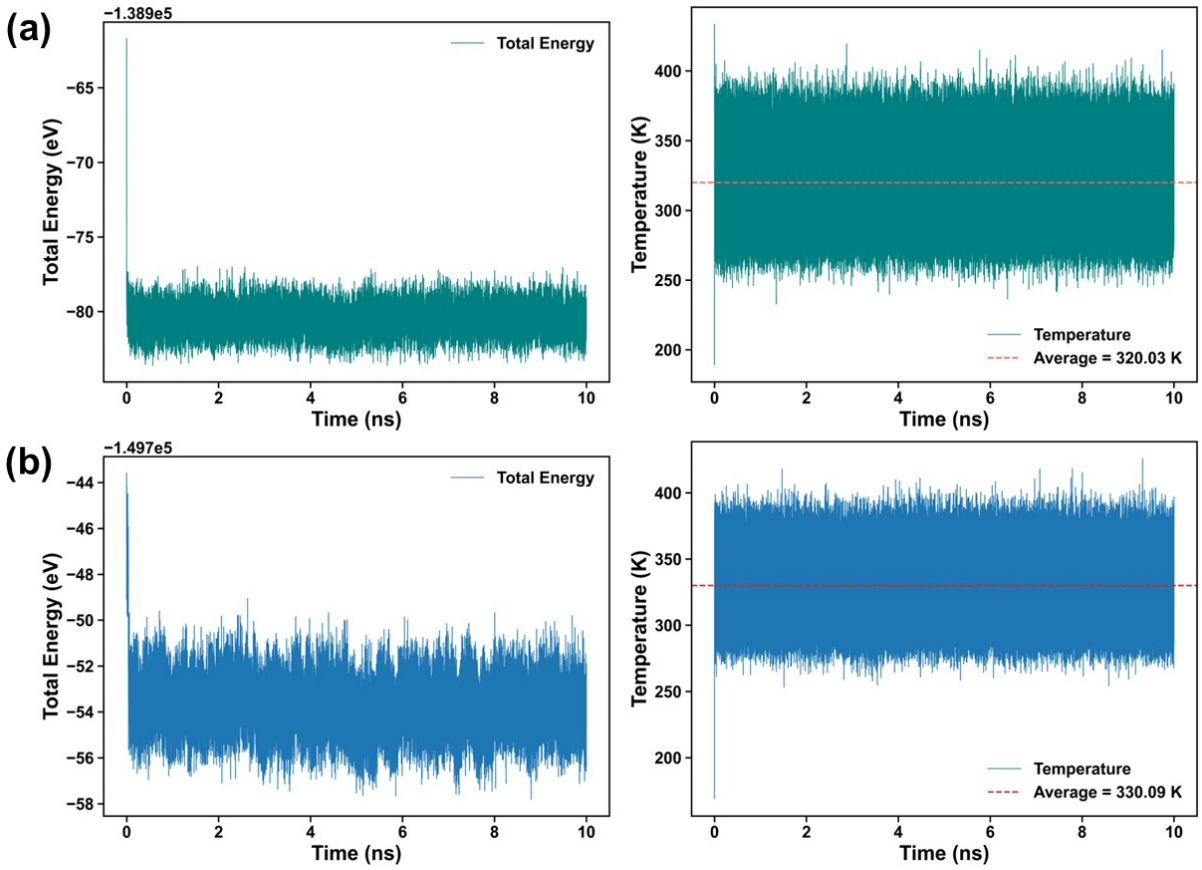

Figure S5: Time evolution of potential energy (left) and temperature (right). Panels (a) and (b) correspond to the (110) and (101) surfaces, respectively, obtained from the 10 ns MLMD simulations.

2.4 MLIP Validation:

The out-of-distribution (OOD) transferability of the trained MLIP models was systematically assessed by benchmarking their predictive performance against independent AIMD datasets generated across a range of temperatures not encountered during training. Specifically, the models were evaluated against independent AIMD datasets generated at 200 K, 400 K, 500 K, and 600 K, none of which were included during MLIP training. As shown in Table S1, the regression metrics (RMSE and MAE for both energies and forces) remain at a reasonably high level of accuracy across all unseen temperatures for both facets. The corresponding parity plots in Figure S6 confirm that the models accurately describe configurations well outside the 330 K training distribution, including highly distorted geometries sampled at 600 K.

Table S1. Regression metrics (RMSE and MAE) for energies and forces predicted by the 330 K AIMD-trained MLIP models evaluated on independent AIMD datasets generated at 200-600 K for the IrO_2 (110) and (101) surfaces.

Temperature	(110) Surface				(101) Surface			
	Energy (meV/Atom)		Force (meV/Å)		Energy (meV/Atom)		Force (meV/Å)	
	RMSE	MAE	RMSE	MAE	RMSE	MAE	RMSE	MAE
200K	0.75	0.64	95.61	72.50	0.36	0.28	89.33	67.12
400K	1.01	0.86	109.20	81.61	0.76	0.62	109.02	81.67
500K	0.88	0.70	119.09	87.70	0.65	0.53	120.80	89.28
600K	0.90	0.71	131.29	96.03	0.75	0.61	133.45	97.68

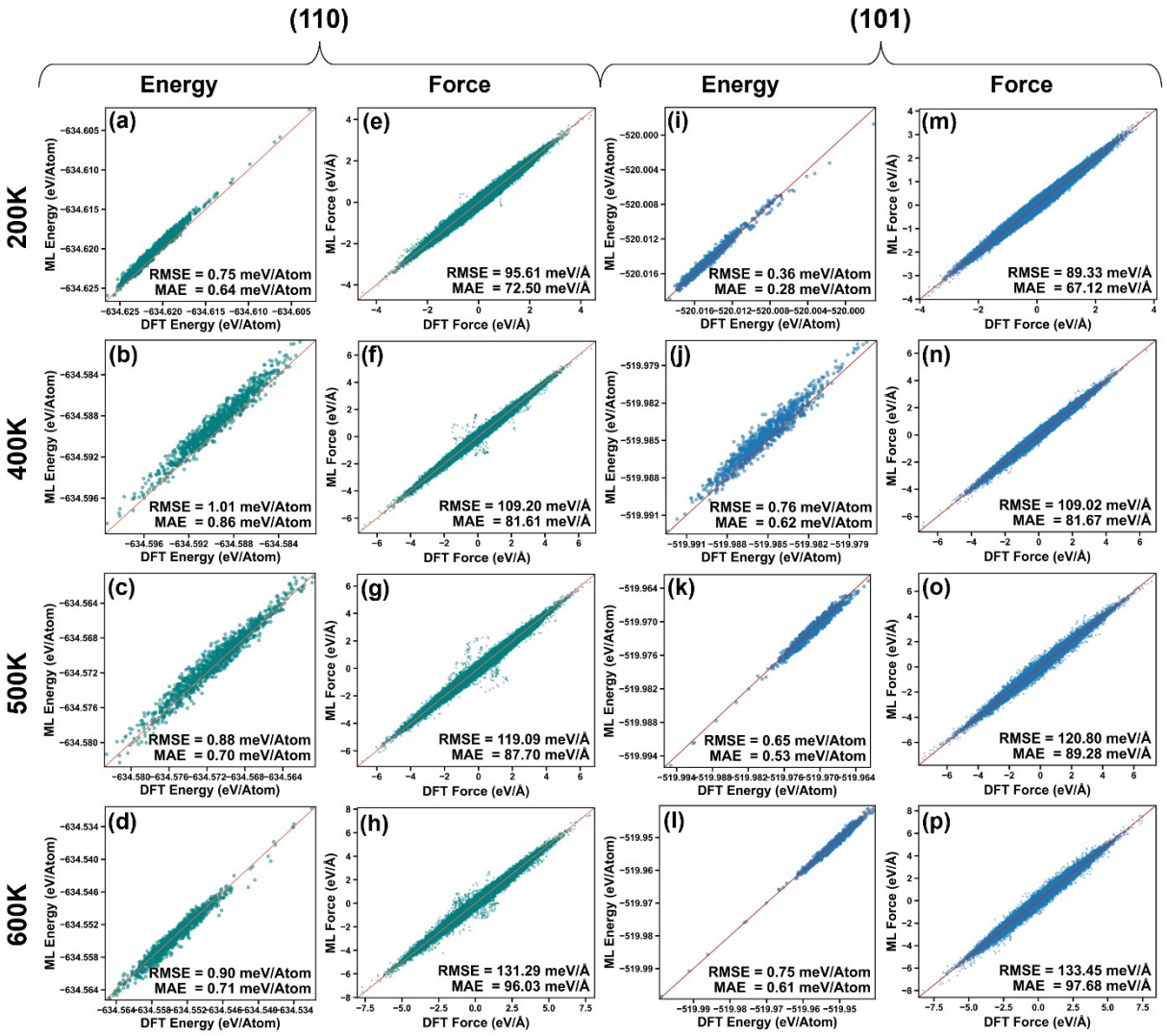

Figure S6. Parity plots of MLIP-predicted energies and forces against DFT reference values for the IrO_2 (110) and (101) surfaces, evaluated on independent AIMD datasets at 200 K, 400 K, 500 K, and 600 K. For the (110) surface, energy and force correlations are shown in panels (a-d) and (e-h), respectively and corresponding panels for the (101) surface are presented in (i-l) and (m-p).

In order to systematically broaden the configurational space sampled during training, an expanded dataset was constructed by incorporating AIMD frames collected at 200 K, 330 K, 400 K, 500 K, and 600 K, supplemented by rattled and strain-displaced structures specifically designed to probe OOD configurations. Starting from randomly selected equilibrated frames from the 330 K AIMD simulation, we carried out short 3 ps AIMD runs at each of these temperatures using the same computational setup as the original 10 ps trajectory. Equi-spaced frames were extracted from these trajectories and for the 330 K simulation only post-equilibration configurations (beyond the initial 2 ps) were included.

Two complementary strategies were employed to further augment the structural diversity of the training set. First, controlled mechanical deformations were applied via strain engineering: biaxial in-plane strain and uniaxial strains along the x and y directions, each spanning a symmetric range of -2% to +2%, generating 18 configurations that capture the materials response under both compression and tension. Second, thermal distortions were introduced through atomic rattling: approximately 30 structures were generated by applying random Gaussian displacements to atomic positions, with displacement magnitudes calibrated by atom type and spatial location (0.050 Å for Ir; 0.050-0.095 Å for O depending on layer; 0.080 Å for H), producing a structurally diverse ensemble that mimics finite-temperature effects. Together, these two strategies contributed approximately 40 distinct structural configurations, enabling systematic exploration of both mechanical and thermal effects. Single-point DFT calculations at the same level of theory as the original AIMD were performed on all generated structures, and these 40 datapoints were incorporated into the expanded training set. The final dataset comprises approximately 7,500-7,600 configurations per facet, with 20% held out as the validation set.

As shown in Figure S7, the models trained on this expanded dataset reproduce DFT energies and forces with high fidelity. Using these retrained MLIPs, we performed extended 10 ns MLMD simulations at 330 K for both facets. As evident from Figure S8, the trajectories remain thermally stable and energetically well-converged throughout the simulation. Critically, the water density profiles, radial distribution functions (RDFs), and vibrational density of states (VDOS) obtained from the expanded model are in excellent agreement with those from the original model trained solely on the 330 K trajectory (see Figure S9). This close agreement confirms that the original 10 ps training trajectory already captures the essential configurational space relevant to 330 K conditions. Consequently, the convergence observed in the 10 ns MLMD simulations reflects physically meaningful behavior rather than an artifact of a limited training distribution.

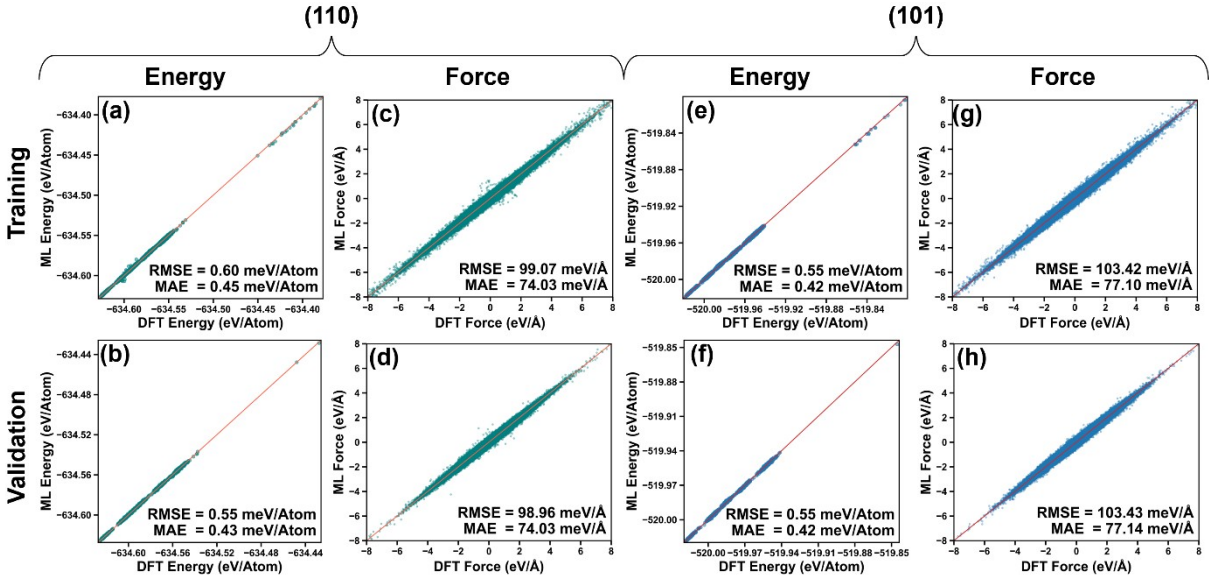

Figure S7. Parity plots of MLIP-predicted versus DFT reference energies and forces for the IrO_2(110) and (101) surfaces, obtained from the expanded training dataset. Panels (a) and (b) show energy correlations for the training and validation sets of the (110) surface, respectively, with the corresponding force correlations presented in panels (c) and (d). Analogous energy and force parity plots for the (101) surface are shown in panels (e), (f) and (g), (h), respectively.

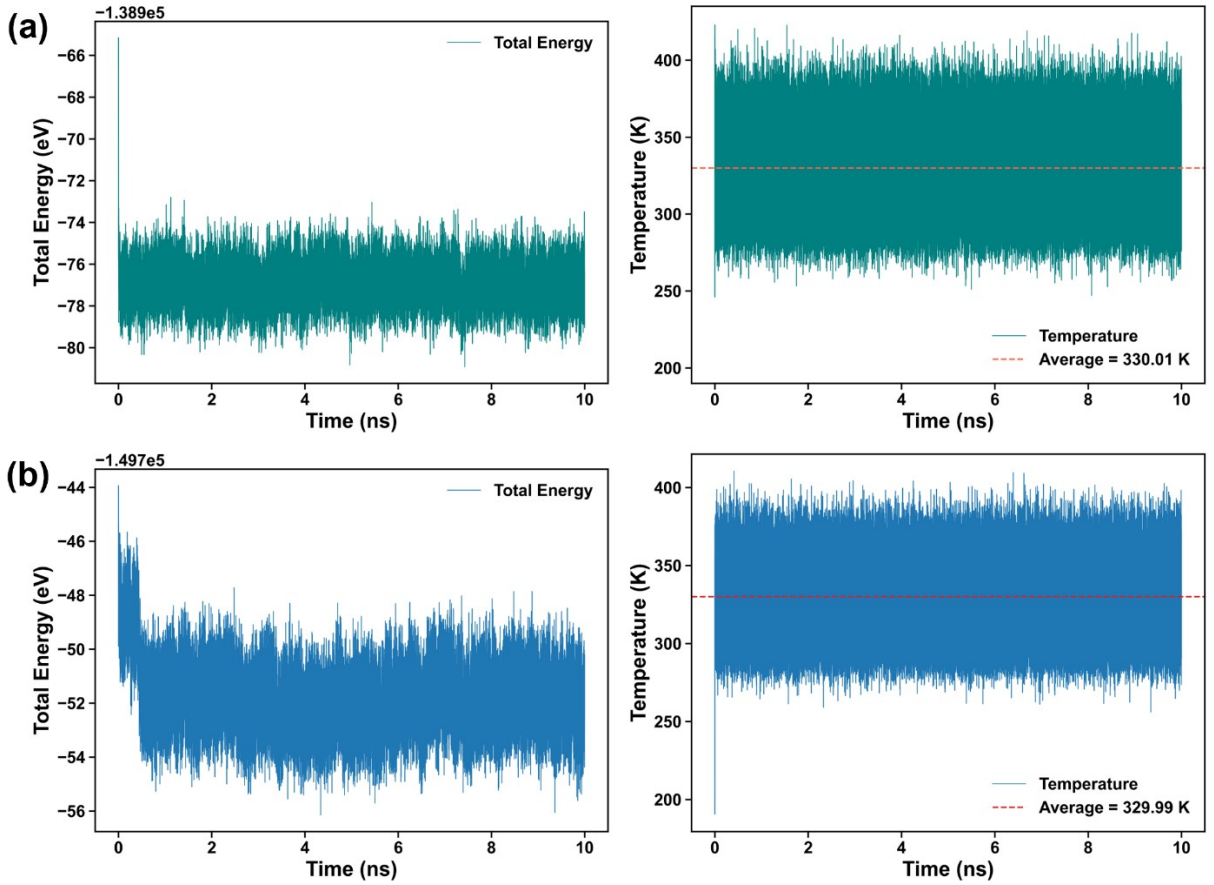

Figure S8: Time evolution of total energy (left) and temperature (right). Panels (a) and (b) correspond to the (110) and (101) surfaces, respectively, obtained from the retrained MLIP-driven 10 ns MLMD simulations.

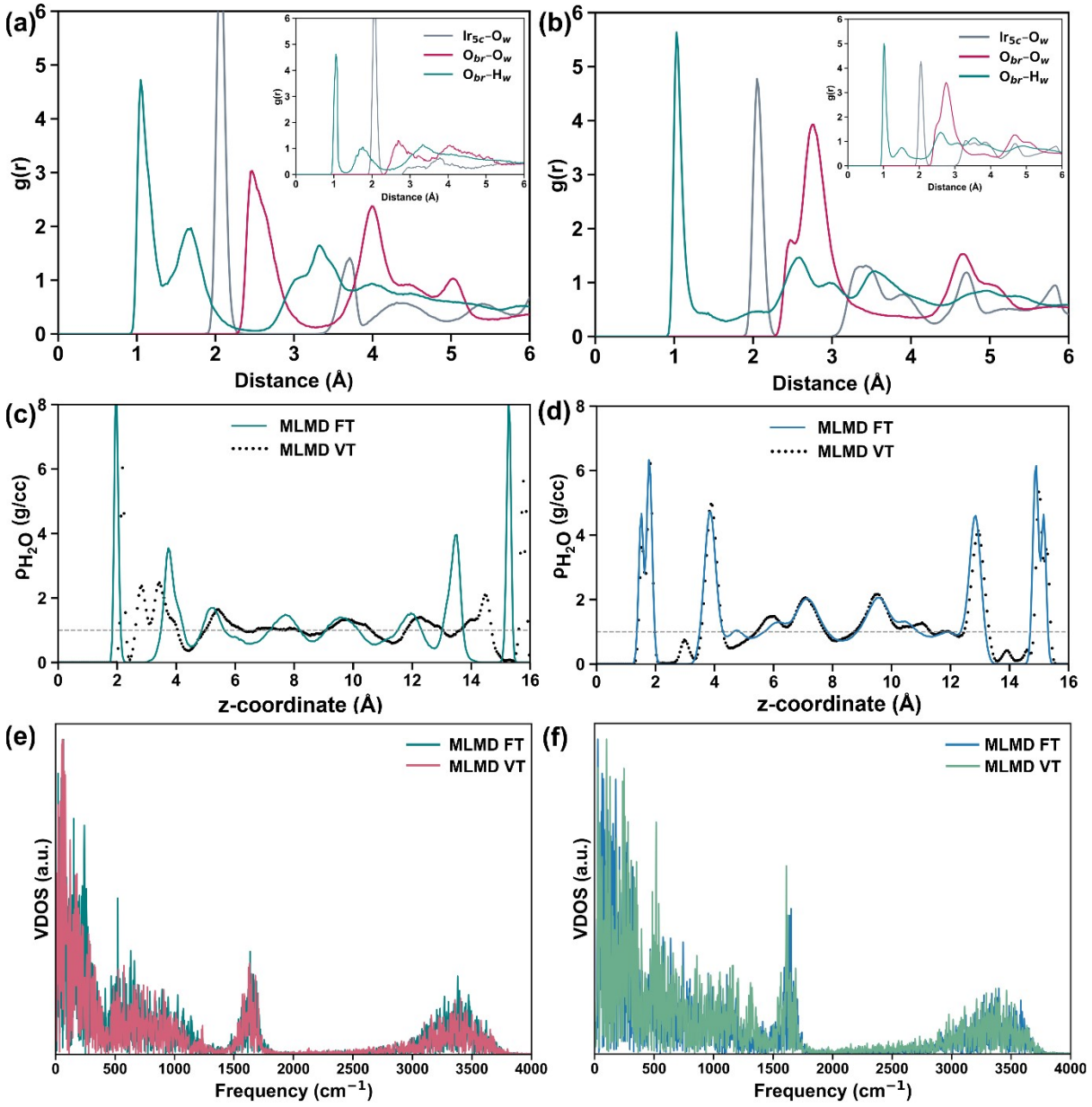

Figure S9: Radial distribution function of selected atomic type pairs at the (a) IrO_2(110)/H2O and (b) IrO_2(101)/H_2O interface obtained from MLMD simulations trained on a fixed, 330 K AIMD dataset (MLMD FT) and from MLMD simulations sampling various temperature AIMD dataset (MLMD VT, inset). Water density profile obtained upon MLMD FT and MLMD VT simulations for IrO_2 (c) (110) and (d) (101) surface. Vibrational density of state (VDOS) profile of the water layers obtained from the MLMD FT and MLMD VT simulation for the (e) (110) and (f) (101) surface.

2.5 CI-NEB Calculation:

For IrO_2 covered with a monolayer of adsorbed water, the climbing-image nudge elastic band (CI-NEB) method, developed by the Henkelman group[13,14], was used to determine the transition state geometries and energy barriers as implemented in the Vienna Ab-initio Simulation Package (VASP) code. The image of the highest energy approximated the transition state of the optimized reaction coordinate.

2.6 OER Profile Calculations:

All the first principle-based static calculations were carried out using the VASP [15–17] program, based on plane-wave basis sets. The Perdew, Burke, and Ernzerhof (PBE) generalized gradient approximation (GGA)[3] was employed for the electronic exchange-correlation function. The electron-ion interactions were used utilizing the all-electron projector augmented wave (PAW)[18] method. A plane-wave cutoff energy of 500 eV and a convergence threshold of 10^{-5} eV in total energy were used for the electronic density. A maximum force of less than 0.02 eV/ Å on any ion and Gaussian smearing with a smearing width of 0.05 eV were employed for the structural optimization. Throughout the calculations, the dispersion correction term was considered using the van der Waals density correction with the IVDW = 11 tag, corresponding to the DFT-D3 method of Grimme with zero-damping function[4]. A Gamma (Γ)-centered k-point grid of 1×1×1 was employed to sample the Brillouin zone for optimization purposes.

The implicit solvation was described using the self-consistent continuum solvation framework, (dielectric constant, ε = 80, and Debye screening length 3.04 Å), coupled with the linearized Poisson-Boltzmann model (PBM) as implemented in VASPsol.[19,20]

Water electrolysis involves the hydrogen evolution reaction (HER) at the cathode and the oxygen evolution reaction (OER) at the anode. Theoretically, a potential difference of 1.23 V is required between the anode and cathode to drive the overall reaction. In OER, molecular oxygen is produced *via* four proton/electron-coupled procedures depending on the pH environment. In acidic conditions, two water molecules are oxidized into four protons (H^+) and an oxygen molecule (O_2).

$$2H_2O_{(l)} \rightarrow 4H^+ + O_{2(g)} + 4e^-$$

It is traditionally taken into account that OER occurs via four electrochemical steps involving the simultaneous release of proton-electron couples. Following the adsorbate evolution mechanism (AEM), upon adsorption on the active surface metal site via a one-electron oxidation process, a water molecule forms a site-adsorbed hydroxyl (*OH) intermediate. Subsequently, *OH undergoes a proton coupling and electron removal to form oxo (*O)

intermediate. The following O-O bond formation step allows *O to react with a second water molecule to form hydro-peroxide (*OOH) species. Finally, *OOH is oxidized by a one-electron transfer process to release O_2 and recover the initial active site. Each elementary step possesses specific free energy as a function of binding energies/adsorption free energy of the corresponding intermediates, given as,

$$\Delta G_{OH^*} = G_{OH^*} + \frac{1}{2}G_{H_2} - G_{H_2O} - G_* - kTln10 \times pH - eU_{SHE} \quad (1)$$

$$\Delta G_{O^*} = G_{O^*} + G_{H_2} - G_{H_2O} - G_* - 2kTln10 \times pH - 2eU_{SHE} \quad (2)$$

$$\Delta G_{OOH^*} = G_{OOH^*} + \frac{3}{2}G_{H_2} - 2G_{H_2O} - G_* - 3kTln10 \times pH - 3eU_{SHE} \quad (3)$$

Furthermore, the free energies of the intermediates were obtained by $G = E_{elect} + ZPE - TS$, where E_{elect} is the electronic energy of the corresponding intermediate, ZPE is the zero-point energy, S is the entropy, and T is the absolute temperature. The ZPE corrections and entropies of intermediates were calculated using vibrational analysis at T = 298.15 K with VASPKIT.[21]

The four-electron steps of the OER pathway in acidic conditions (pH = 0) can be broken down as in the computational hydrogen electrode (CHE) model, introduced by Nørskov *et al.*[22]

$$* + H_2O_{(l)} \rightarrow OH^* + H^+ + e^- \; ; \; \Delta G_{CHE}^{1} = \Delta G_{OH^*} + \Delta G_U \quad (4a)$$

$$OH^* \rightarrow O^* + H^+ + e^- \; ; \; \Delta G_{CHE}^{2} = \Delta G_{O^*} - \Delta G_{OH^*} + \Delta G_U \quad (4b)$$

$$O^* + H_2O_{(l)} \rightarrow OOH^* + H^+ + e^- \; ; \; \Delta G_{CHE}^{3} = \Delta G_{OOH^*} - \Delta G_{O^*} + \Delta G_U \quad (4c)$$

$$OOH^* \rightarrow O_{2(g)} + H^+ + e^- \; ; \; \Delta G_{CHE}^{4} = \Delta G_{O_2}(= 4.92eV) - \Delta G_{OOH^*} + \Delta G_U \quad (4d)$$

The ΔG_U is the potential correction term.

To drive the OER, a minimal theoretical voltage of 1.23 V is needful at room temperature. However, practical operation demands a higher applied potential to drive the reaction at appreciable rates. From a thermodynamic standpoint, such a biasing potential exceeding the minimum of 1.23 V can drive these four steps exothermically and is termed as overpotential. The step with the largest free energy difference is defined as the rate-limiting step and regulates the theoretical overpotential of the whole reaction. Given as,

$$\eta_{CHE}^{OER} = \frac{\{\Delta G_{CHE}^{i}\}}{e} - 1.23\text{V} \quad (5)$$

Each reaction intermediate was optimized in the presence of an equilibrated interfacial water layer captured from the MLMD simulation, thereby capturing the dynamic solvation effects that conventional static or implicit models often overlook.

2.7 Electronic Structure Analysis Calculations:

Work function (φ) calculations were initially performed for the pristine IrO_2 slab model in vacuum to characterize the intrinsic electronic properties of the two facets under study. φ was defined as the difference between the electrostatic potential in the vacuum region and the Fermi level of the slab. The vacuum reference was determined from the plane-averaged electrostatic potential along the surface normal direction (z-axis). Further, to assess the influence of solvation, the water-equilibrated surface structures were considered for the study. Solvent-induced electronic effects were analyzed by monitoring shifts in the Fermi level and changes in the plane-averaged electrostatic potential relative to the vacuum-referenced pristine slab models. These potential shifts capture interfacial charge redistribution and solvent-induced screening at the solid-liquid interface.

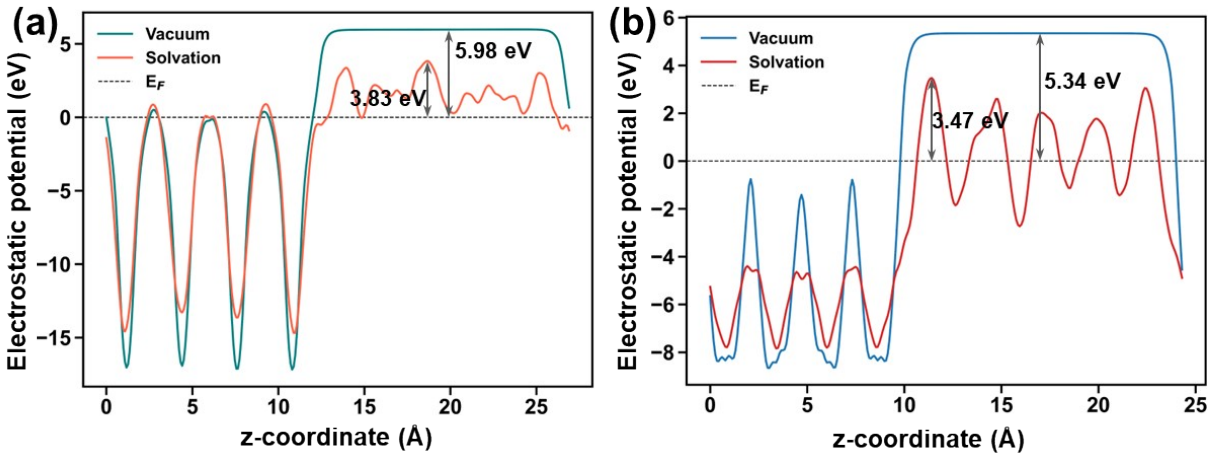

Figure S10: Planar-averaged electrostatic potential profiles along the surface normal (z-axis) for the IrO_2 (a) (110) and (b) (101) surfaces under vacuum and explicit solvation conditions. The electrostatic potentials are referenced to the Fermi level (E_F = 0 eV) (dashed line). The vacuum level is identified from the plateau region in the vacuum, while in the solvated system the oscillatory behaviour reflects the structured solvent layers and interfacial electrostatic screening at the IrO_2/H_2O interface.

The electronic structure of the catalyst surface of interest was further analyzed for configurations with an adsorbed oxygen-based intermediate. Orbital-resolved ***projected density of states (PDOS)*** calculations was performed to evaluate the contributions of the Ir(5d) states and O(2p) states in the vicinity of the Fermi level, providing insight into the extent of metal-oxygen hybridization under adsorbed conditions. All PDOS spectra were referenced to the Fermi level, set at 0 eV.

The d-band center (ε_d) plays a crucial role as a quantitative descriptor in determining the strength of interactions between the active catalytic metal site and adsorbed molecules, which

directly channels the catalytic activity. The position of the ε_d is determined with the formula, $\varepsilon_d = \int \frac{E\rho(E)dE}{\rho(E)dE}$, where E represents the energy of the d-electrons, $\rho(E)$ denotes the density of states for the d-orbitals. [23–25]

Furthermore, to examine the charge redistribution between the catalytically active Ir site and the O-containing adsorbed intermediates, ***Bader charge*** and Bader population analyses were performed using the Henkelman Group's Bader analysis program. [26–28] Alongside, the charge density differences of the key OER intermediates were mapped using the VASPKIT program.

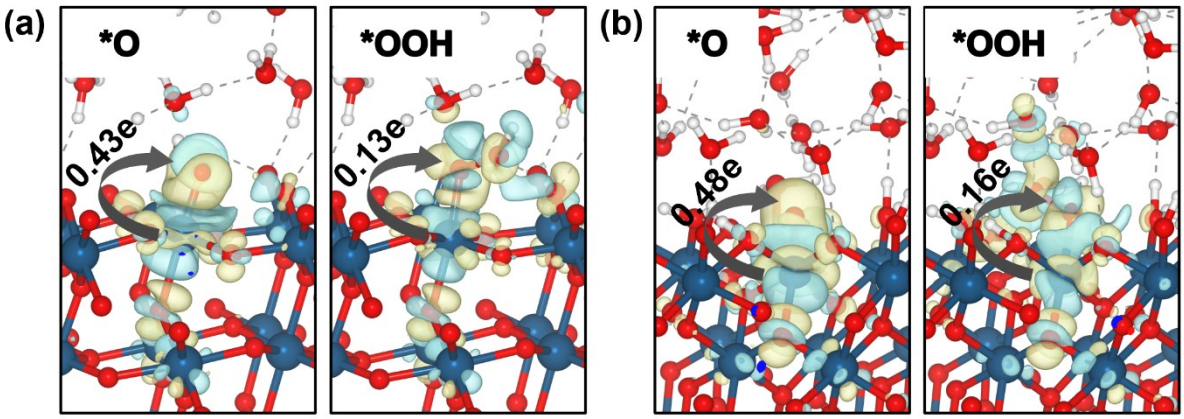

Figure S11: Charge density difference (CDD) plots for the *O (left panels) and *OOH (right panels) intermediates on (a) IrO_2(110) and (b) IrO_2(101) facets, computed under explicit water solvation. Yellow and cyan iso-surfaces denote charge depletion and accumulation, respectively, with an iso-value of 0.0025 eÅ^{-3}. The arrows indicate the net Bader charge transfer from the Ir_{5c} active site to the adsorbed intermediate.

Lastly, ***the Crystal Orbital Hamiltonian Population (COHP)***[29] calculations were performed using the LOBSTER [30] package, starting from converged and relaxed electronic structures. The orbital-resolved COHP and integrated COHP (ICOHP) between metal d-orbitals and oxygen 2p-orbitals were investigated to understand the bonding strength between the catalyst and the target OER intermediates. The ICOHP analysis also provides a significant insight into bonding and antibonding interactions, rather than orbital population, as in the case of the density of states (DOS) calculation.

3. Surface Structure Coordinates:

IrO_2-110

IrO2_110

1.00000000000000

6.3534002304079999 0.0000000000000000 0.0000000000000000

0.0000000000000000 12.7430000305179991 0.0000000000000000

0.0000000000000000 0.0000000000000000 26.9953994750980009

Ir O

32 64

Direct

0.0015761122128599 0.2566653586245330 0.0451285671117891

0.0016886258135999 0.0026351105844442 0.1661281359335437

0.0017767060097874 0.2508982946665760 0.2821635489982973

0.0004569992319237 0.9841381246653790 0.4012712305357093

0.2518074764734627 0.0058263293020690 0.0475383570376051

0.2520356659242654 0.2521344588032084 0.1641190216094452

0.2516847230182686 0.0008567714633883 0.2831203450343857

0.2504748374338449 0.2348490209971387 0.4004185711535285

0.5015980500109175 0.2566793609747745 0.0451174669904629

0.5016926568893864 0.0026190126183406 0.1661264773298450

0.5017730910769810 0.2509088998860002 0.2821675760529899

0.5004576576606222 0.9841340760277654 0.4012811846044117

0.7518064580842341 0.0058168862423419 0.0475419003042403

0.7520425671183569 0.2521348570614697 0.1641219317516953

0.7516866944961957 0.0008612717653363 0.2831177859207110

0.7504696422027296 0.2348456766836935 0.4004136758415214

0.0011680756488656 0.7545931945193171 0.0447627405968856

0.0016616096771783 0.5024365191412692 0.1587501931934276

0.0015630922323462 0.7495462778111902 0.2822429730446255

0.0001801954697372 0.4844183474873602 0.3974955448718199

0.2518408767154259 0.5058901815486143 0.0406353386284337

0.2520343775668668 0.7540868843135947 0.1639050464273069

0.2513032651618167 0.5006239700305053 0.2782926474457562

0.2505420623557024 0.7344819152079420 0.4006896584533191

0.5011759253689422 0.7545868796380512 0.0447627309870102

0.5016570082996333 0.5024219756215966 0.1587567173465547

0.5015647553529240 0.7495553977397442 0.2822419201163591

0.5001719343436835 0.4844256978138407 0.3975046038294288

0.7518368078575126 0.5058815344965167 0.0406359831839080
0.7520290251431230 0.7540848848113667 0.1639071241239119
0.7513065049255705 0.5006274017101493 0.2782897272794713
0.7505461523858079 0.7344708144921879 0.4006856357186070
0.2515908815510896 0.3480676708696695 0.0399723825151185
0.2518051179552333 0.0965319735402661 0.1687949900947561
0.2515288789079299 0.3455832347389631 0.2842384345966388
0.2504370766451353 0.0779542606261156 0.4037485745213447
0.2515271588592683 0.1625050229456433 0.0457567456500940
0.2514175879683266 0.4072043616078481 0.1568129375195769
0.2521432667306637 0.1571164264298047 0.2789283069058356
0.2502193856686004 0.3923485547765522 0.3994631387452962
0.0017324932682622 0.0059698269655495 0.0919975836754392
0.0022357965808914 0.2656471825868721 0.2086175537645072
0.0016293707898837 0.0191699560302838 0.3271698877598713
0.0001276577161553 0.2350921821226324 0.4433071782856993
0.0019596829862881 0.0055147872289293 0.0045394461352738
0.0020764213204235 0.2314918643273006 0.1203045733841911
0.0016033612753363 0.9896671121341349 0.2390934911799702
0.0008351247836035 0.2381971976944988 0.3558832914679209
0.7516371849312659 0.3480851274268857 0.0399792966884628
0.7517762374589352 0.0965305086432745 0.1688053966267346
0.7515505628485176 0.3455934381483597 0.2842311533944483
0.7504882236521202 0.0779758995245284 0.4037309164833254
0.7515224733474891 0.1625061848581928 0.0457560698916621
0.7514379723858435 0.4072021725043229 0.1568166300425571
0.7521499580477109 0.1571281181037002 0.2789322976343160
0.7502121123929130 0.3923619069689974 0.3994452878807855
0.5017414134600032 0.0059052270384717 0.0919897317052039
0.5022594397546691 0.2657897030817714 0.2086251767477740
0.5016145183038616 0.0191948830595481 0.3271640535472590
0.5001488778899891 0.2351113367135622 0.4433074702940623
0.5019711557878571 0.0055199048048980 0.0045379411602629
0.5021196535376644 0.2316325536193144 0.1203150288001616

0.5016067018602081 0.9896714394850864 0.2390946667925578
0.5008653754758969 0.2382010258268854 0.3558797044346504
0.2512598520614956 0.8488974646965975 0.0457360461342524
0.2520219674143124 0.5976139058283620 0.1593182887011838
0.2514290676012889 0.8443995479960063 0.2848733477118313
0.2502992923398279 0.5781113718121328 0.4003857559692889
0.2513143872399920 0.6631830627106042 0.0394046822042080
0.2515818242865168 0.9091846921446225 0.1659757410469385
0.2517068088630213 0.6562390099452416 0.2788504784204792
0.2503898629991692 0.8919140932846817 0.4031170301984944
0.0019211336969099 0.5060693258676081 0.0851521368674207
0.0020058225953615 0.7426578586020678 0.2084858393807493
0.0010159509381367 0.5163121619150728 0.3226795229821528
0.0006610821248139 0.7308659964854742 0.4435887280624942
0.0018986960769409 0.5054852049543573 0.9977498419348253
0.0020951198610491 0.7751417211456435 0.1201095218246983
0.0012700163019066 0.4914426348701493 0.2331682817429052
0.0006255850237876 0.7405736381724713 0.3562397505283370
0.7512473472830132 0.8488883625201963 0.0457472798639612
0.7519395840360734 0.5976108520476311 0.1593058586456624
0.7514203744306288 0.8444054243159099 0.2848661979069849
0.7502770642443234 0.5781066778419549 0.4003886767681210
0.7512765082023268 0.6631940203495953 0.0394172952567935
0.7516347039800497 0.9091885477914315 0.1659747963022923
0.7516924750411881 0.6562353052322485 0.2788486564727852
0.7504353912804527 0.8919251864523871 0.4030701556460133
0.5018904265443026 0.5060465182009692 0.0851480632547434
0.5019553858810092 0.7427254153619407 0.2084933366398925
0.5010415979580426 0.5163076926200708 0.3226779838962369
0.5006715330449978 0.7308427925998332 0.4435850161336014
0.5018919196299388 0.5054738342212378 0.9977387804912002
0.5020350213248314 0.7751936487769658 0.1201079423241661
0.5012579382132697 0.4914472214107252 0.2331660682436243
0.5005791920396404 0.7405602775109039 0.3562368196594125

IrO_2-101

IrO2_101

1.00000000000000

11.0253000259400000 0.0000000000000000 0.0000000000000000

0.0000000000000000 9.0106000900269994 0.0000000000000000

0.0000000000000000 0.0000000000000000 24.3913993835450000

Ir O

32 64

Direct

0.4994731018744072 0.9881606901683286 0.0315621425062257

0.3309806198283525 0.0023184298622082 0.1385442004537524

0.1670477632170754 0.9984859057071678 0.2469747005274550

0.9980937068120208 0.0129474039605323 0.3538925735878750

0.2495961087248932 0.2627202743936686 0.0318641130726236

0.0814874799250206 0.2478836486918024 0.1388143940895981

0.4171806196825762 0.2528679596688082 0.2469464316379329

0.2480131509879781 0.2388597825659874 0.3537516293704673

0.9997834698441723 0.9883734383411885 0.0316633462024155

0.8313163544644896 0.0033437042410491 0.1387542509190637

0.6664876815292831 0.9978587933339967 0.2467987669771952

0.4979289385260792 0.0127588689220454 0.3539259049939121

0.7497672389562626 0.2623793766758862 0.0318210648685539

0.5806001130855609 0.2481496506249777 0.1386089021869678

0.9166234332173600 0.2529007404883059 0.2467638231933715

0.7480067813459683 0.2384090428520577 0.3537066688053108

0.4997648379272904 0.4883529388818291 0.0316447396003620

0.3313008527287824 0.5033704676336705 0.1387663401940846

0.1664874680120482 0.4978827262359585 0.2468033229737975

0.9979811698023128 0.5127722092367757 0.3539330594063411

0.2497684230223028 0.7622972867146783 0.0317958891092842

0.0805988193474927 0.7481905800486005 0.1386314606772813

0.4166257236815151 0.7528813803632349 0.2467648647876507

0.2480450534805434 0.7384276576114287 0.3537197716872635

0.9995442188330806 0.4883708797287685 0.0316088126952623
0.8309658815409398 0.5022932428521740 0.1385763729864246
0.6669918993823424 0.4984503785872332 0.2469717393174929
0.4981387747550672 0.5129786151300206 0.3538976119130698
0.7496383938718790 0.7626864683173225 0.0318921486083219
0.5814818923081405 0.7478264103943978 0.1388162310393858
0.9171867485292144 0.7528630516597304 0.2469513258058999
0.7480328123976450 0.7388738391654247 0.3537403124278934
0.1393065380137883 0.4021383368765430 0.0001432071506330
0.4830634776224232 0.4120348874005908 0.1085958036066209
0.3166940856347680 0.4095911007819554 0.2136016084582482
0.1472303268204386 0.4051678129271936 0.3218000234377698
0.3506816921730243 0.0969176418625662 0.0638362417954942
0.1871739173707315 0.1000551825705104 0.1738196008208731
0.0252385335274682 0.1037841480147114 0.2798848304553866
0.3590970457035213 0.1002481085625218 0.3854816597389132
0.3886847553265058 0.3500583851173480 0.0002691001989267
0.2287517301931913 0.3462111915862081 0.1075447008867304
0.0629624435239054 0.3474696599643243 0.2124127278807318
0.3975415842404942 0.3478079309517795 0.3214519821156295
0.1018754427893263 0.1528430201124535 0.0641341173615656
0.4333494823896356 0.1554583482835930 0.1722599320415217
0.2707833351863278 0.1545402456121035 0.2783654470780212
0.1095856411452241 0.1517322029365393 0.3857104436771047
0.6388278861588794 0.4011083294295005 0.0001808502727842
0.9725723661973324 0.3965680031938105 0.1054793040577813
0.8112667888181241 0.4011548990506394 0.2119231988207973
0.6461495112205565 0.4032181705089106 0.3214470328544830
0.8505023892772503 0.0963728161179294 0.0637614372108925
0.6812939107362459 0.0917467643486040 0.1720753244049550
0.5146734116907089 0.0888666727416219 0.2769161716246244
0.8587301539835265 0.0995562102351520 0.3855078814450967
0.8880638254128853 0.3496969997352126 0.9997433520966477
0.7279506174536698 0.3450623554353874 0.1075346864151152

0.5642620208589159 0.3458658764984318 0.2132054645640802
0.8965006243727858 0.3474638423898606 0.3215112197722111
0.6001634325118353 0.1531091843025878 0.0641405360116507
0.9350250890692814 0.1535143239334557 0.1731151686724785
0.7696290079221364 0.1540470857481340 0.2782553201673515
0.6087951603203353 0.1513295942578569 0.3853565608255036
0.1388218128291880 0.9011279354405887 0.0002005617329921
0.4725205037619185 0.8964147653924533 0.1054759756372274
0.3113104740315477 0.9012245138425199 0.2119130520343334
0.1461377204172613 0.9031964447814279 0.3214449631373254
0.3504809545549142 0.5962769563077187 0.0637679003633141
0.1812571252149401 0.5917479344440971 0.1720824874840323
0.0147585825564099 0.5890177174066826 0.2769408364602339
0.3588131773365099 0.5996926491391291 0.3855208073572788
0.3880817711607757 0.8494028514125056 0.9996011149548274
0.2279766812163665 0.8450188993235521 0.1075309597498003
0.0642660712076939 0.8459256603487001 0.2132176300911584
0.3964715494765413 0.8474722429604663 0.3214990983164294
0.1001174023485905 0.6532879360924271 0.0641512790465489
0.4350183948193946 0.6535079023036148 0.1731169608621737
0.2696327364940395 0.6540555542822137 0.2782693671962618
0.1089176954461185 0.6512168528620577 0.3853859266486440
0.6392962480235918 0.9019976128966478 0.0001311509347770
0.9830365180403320 0.9120528994207763 0.1086113965562810
0.8166928525395692 0.9095773190619619 0.2135941821820012
0.6472075334910695 0.9051470729678459 0.3217886487480063
0.8507969237450282 0.5970709154371875 0.0639420391045841
0.6870642850608716 0.5998376664400367 0.1738062507790448
0.5252664772293693 0.6037787211195784 0.2798980838320375
0.8590920725605596 0.6002525485904350 0.3854733373936912
0.8887238369713132 0.8500372953591804 0.0002991931195199
0.7287955007146601 0.8461082066010429 0.1075657004372268
0.5629454628021060 0.8474547169825289 0.2124255542383093
0.8975222992517693 0.8478017589465172 0.3214414333367993

0.6019190107321097 0.6527824754374647 0.0641409509129400
0.9332771734035493 0.6555433721745060 0.1722792076261096
0.7707528395889339 0.6545441042928551 0.2783355164887414
0.6096324430642407 0.6517458825333733 0.3857182949587566

4. References:

1 J. VandeVondele, M. Krack, F. Mohamed, M. Parrinello, T. Chassaing and J. Hutter, *Comput. Phys. Commun.*, 2005, **167**, 103–128.

2 J. Hutter, M. Iannuzzi, F. Schiffmann and J. VandeVondele, *WIREs Computational Molecular Science*, 2014, **4**, 15–25.

3 J. P. Perdew, K. Burke and M. Ernzerhof, *Phys. Rev. Lett.*, 1996, **77**, 3865–3868.

4 S. Grimme, J. Antony, S. Ehrlich and H. Krieg, *J. Chem. Phys.*, DOI:10.1063/1.3382344.

5 S. Goedecker, M. Teter and J. Hutter, *Phys. Rev. B*, 1996, **54**, 1703–1710.

6 C. Hartwigsen, S. Goedecker and J. Hutter, *Phys. Rev. B*, 1998, **58**, 3641–3662.

7 J. VandeVondele and J. Hutter, *J. Chem. Phys.*, DOI:10.1063/1.2770708.

8 S. Nosé, *J. Chem. Phys.*, 1984, **81**, 511–519.

9 H. Wang, L. Zhang, J. Han and W. E, *Comput. Phys. Commun.*, 2018, **228**, 178–184.

10 J. Zeng, D. Zhang, D. Lu, P. Mo, Z. Li, Y. Chen, M. Rynik, L. Huang, Z. Li, S. Shi, Y. Wang, H. Ye, P. Tuo, J. Yang, Y. Ding, Y. Li, D. Tisi, Q. Zeng, H. Bao, Y. Xia, J. Huang, K. Muraoka, Y. Wang, J. Chang, F. Yuan, S. L. Bore, C. Cai, Y. Lin, B. Wang, J. Xu, J.-X. Zhu, C. Luo, Y. Zhang, R. E. A. Goodall, W. Liang, A. K. Singh, S. Yao, J. Zhang, R. Wentzcovitch, J. Han, J. Liu, W. Jia, D. M. York, W. E, R. Car, L. Zhang and H. Wang, *J. Chem. Phys.*, DOI:10.1063/5.0155600.

11 Linfeng Zhang, Jiequn Han, Han Wang, Wissam A. Saidi, Roberto Car and Weinan E, *Adv. Neural Inf. Process. Syst.*, 2018, **2018-December**, 4436–4446.

12 A. P. Thompson, H. M. Aktulga, R. Berger, D. S. Bolintineanu, W. M. Brown, P. S. Crozier, P. J. in 't Veld, A. Kohlmeyer, S. G. Moore, T. D. Nguyen, R. Shan, M. J. Stevens, J. Tranchida, C. Trott and S. J. Plimpton, *Comput. Phys. Commun.*, 2022, **271**, 108171.

13 G. Henkelman, B. P. Uberuaga and H. Jónsson, *J. Chem. Phys.*, 2000, **113**, 9901–9904.

14 G. Henkelman and H. Jónsson, *J. Chem. Phys.*, 2000, **113**, 9978–9985.

15 G. Kresse and J. Hafner, *Phys. Rev. B*, 1993, **47**, 558–561.

16 G. Kresse and J. Furthmüller, *Phys. Rev. B*, 1996, **54**, 11169–11186.

17 G. Kresse and J. Furthmüller, *Comput. Mater. Sci.*, 1996, **6**, 15–50.

18 G. Kresse and D. Joubert, *Phys. Rev. B*, 1999, **59**, 1758–1775.

19 K. Mathew, R. Sundararaman, K. Letchworth-Weaver, T. A. Arias and R. G. Hennig, *J. Chem. Phys.*, DOI:10.1063/1.4865107.

20 K. Mathew, V. S. C. Kolluru, S. Mula, S. N. Steinmann and R. G. Hennig, *J. Chem. Phys.*, DOI:10.1063/1.5132354.

21 V. Wang, N. Xu, J.-C. Liu, G. Tang and W.-T. Geng, *Comput. Phys. Commun.*, 2021, **267**, 108033.

22 J. K. Nørskov, J. Rossmeisl, A. Logadottir, L. Lindqvist, J. R. Kitchin, T. Bligaard and H. Jónsson, *J. Phys. Chem. B*, 2004, **108**, 17886–17892.

23 B. Hammer and J. K. Nørskov, *Surf. Sci.*, 1995, **343**, 211–220.

24 S. Bhattacharjee, U. V. Waghmare and S.-C. Lee, *Sci. Rep.*, 2016, **6**, 35916.

25 J. K. Nørskov, F. Studt, F. Abild-Pedersen and T. Bligaard, *Fundamental Concepts in Heterogeneous Catalysis*, Wiley, 2014.

26 G. Henkelman, A. Arnaldsson and H. Jónsson, *Comput. Mater. Sci.*, 2006, **36**, 354–360.

27 E. Sanville, S. D. Kenny, R. Smith and G. Henkelman, *J. Comput. Chem.*, 2007, **28**, 899–908.

28 W. Tang, E. Sanville and G. Henkelman, *Journal of Physics: Condensed Matter*, 2009, **21**, 084204.

29 V. L. Deringer, A. L. Tchougréeff and R. Dronskowski, *J. Phys. Chem. A*, 2011, **115**, 5461–5466.

30 R. Nelson, C. Ertural, J. George, V. L. Deringer, G. Hautier and R. Dronskowski, *J. Comput. Chem.*, 2020, **41**, 1931–1940.